

An Eulerian Lagrangian Scheme for Solving Large Deformation Fluid Structure Interaction Problems

James E. Guilkey^a, Todd B. Harman^a, Bryan A. Kashiwa^b and Patrick A. McMurtry^a

^a*Dept. of Mechanical Engineering, University of Utah, Salt Lake City, UT*

^b*Theoretical Division, Los Alamos National Laboratory, Los Alamos, NM*

Abstract

An approach to solving tightly coupled, large deformation, fluid structure interaction problems is presented. The approach uses a theoretical model for the averaged behavior of multiple materials, called the “multifield model”. Solutions to the multifield model equations are obtained using a scheme that combines a Lagrangian technique called the “Material Point Method” with a multifield Eulerian method. In this scheme, the thermodynamic state of each field is integrated forward in time using one of two frames of reference. Embedded structures are integrated in the Lagrangian frame, fluids are integrated in the Eulerian frame. The MPM divides a solid structure into a collection of finite masses and uses a computational grid to affect the update of their states in the Lagrangian frame. A common reference frame is required for evaluation of the interactions associated with exchange of mass, momentum, and energy among fields; for these interactions, the Eulerian frame is chosen. The theoretical model is outlined briefly and the numerical scheme is described in detail. Findings from a numerical order of accuracy study are presented. Results from simulations of three different scenarios are compared with corresponding known solutions to validate the approach. Finally a demonstration calculation is presented to illustrate some of the unique capabilities of the approach.

1 Introduction

The work presented here describes a theoretical and numerical approach for “full physics” dynamic simulations of fluid structure interactions involving large deformations and material transformations (like phase change). By “full physics” we refer to problems involving strong interactions between the fluid field and solid field temperatures and velocities, with a full Navier Stokes

representation of fluid materials and the transient, nonlinear response of solid materials. These interactions may include chemical or physical transformation between the solid and fluid fields.

There are two classes of theoretical models in common use for full physics FSI problems: one considers separated materials, and the other considers their behavior on average. The former is separated in the sense that each material is permitted to occupy some part of space, to the total exclusion of any other material. Interactions among materials can take place only at boundaries between materials, across which there is no flow. In the averaged model, any material can occupy a point in space with some finite probability; hence interactions among materials can take place anywhere. For brevity, we shall call the first model the “separated” model, and the second will be called the “averaged” model.

Numerical solutions to the separated model have been obtained in various approximations, the first of which is often called uncoupled. In this, the load on a structure is estimated from a fluid simulation (or data) and is applied as a boundary condition in a computer simulation of the structural response to the load. This is uncoupled because the response does not (appropriately) change the load. In the next approximation, the velocity of the structural response is permitted to feed back to the fluid simulation, which changes the load. In either approximation the fluid and the structure are retained in separate spatial domains, which are mated at a common boundary where the load/velocity data are shared. Details of the mating process vary among implementations [?]. Regardless of the details, each of these approximations requires exactly one set of state variables in each of their separate domains.

Numerical solutions to the averaged model require one set of state variables for *each* of the materials everywhere in the domain. The averaged model effectively forces the variation in state (which includes the material mass per unit of total volume) to be continuous. Hence a precise interface between materials is not defined, rather, the effect of an unresolved interface is computed on average.

The relative merits of the two models is frequently judged by the robustness of their very different numerical solutions, rather than their accuracy or their ability to address a wide range of physical scenarios. In the separated model, accurate solutions for the structure can be obtained using commercially available simulation tools based on finite element methods. A simple code coupling routine performs the boundary mating with Arbitrary Lagrangian Eulerian (ALE) codes for the fluid part of the domain. Examples of such approaches are widespread, (see [?,?,?,?]). Among the handicaps of this type of approach is that a large distortion of the solid domain can lead to catastrophic mesh tangling. Physical transformations, e.g., phase change,

J2
Need
ref,
Fed-
kew,
JCP

between separated materials is generally beyond the capabilities of this type of approach.

Solutions to the averaged model on an Eulerian grid permit arbitrary distortion, but can suffer from numerical errors that are catastrophic for the solid material. This is because the solid material’s time dependent stress tensor must be transported through the Eulerian grid, and small numerical errors in the transport can lead to highly nonphysical stresses (such as crossing a failure surface artificially). Among the numerical schemes used with the averaged model are those where surface tracking is used to distinguish the interface between materials, but within a multifield description. This widely used approach for mixed material problems often uses the multi-material equations derived from mixture theory ideas originating in the 1960’s, as, for example, described by Soo.[?]. The simulation approach described by McGlaun and Thompson[?] fits into this classification as do the, multi-material interaction simulations of the microstructure of heterogeneous materials described by Benson[?,?]. Typically, surface tracking is used along with a single velocity approximation to minimize material transport errors, but this does not mitigate the undesirable artifacts of stress transport.

The approach described in this paper uses the averaged model, and addresses the issue of stress transport by integrating the state of the solid field in a frame of reference that follows the center of mass motion of the solid field. In this “material” frame, the transport of the stress is error free. Furthermore, the Material Point Method permits the solid field to undergo arbitrary distortion. Because the fluid state is integrated on the Eulerian frame it too can undergo arbitrary distortion. If the rate of momentum exchange is infinitely fast, the single velocity limit is obtained, and the interface region between material fields can be limited to at most a few grid cells. Hence in the differential limit, the separated model is recovered. This means that with sufficient grid resolution, the accuracy of the separated model and the robustness of the averaged model can be obtained simultaneously.

The paper is organized as follows: In Sec. 2, a brief development of the multifield model that forms the foundation of the approach is presented. In Sec. 3 Eulerian and Lagrangian aspects of the solution scheme are described individually. A unique aspect of the approach is the ability to describe the chosen materials in either an Eulerian or Lagrangian frame. In the Lagrangian frame, we use a version of the scheme known as the Material Point Method which is reviewed in Sec. 3.2. The manner in which interactions among fields is accomplished is illustrated in Sec. 3.3. Results from several validation calculations are presented in Sec. 4, followed by a “full physics” demonstration calculation in Sec. 5. Finally, conclusions are made in Sec. 6 including a discussion of some of the strengths and weaknesses of the FSI approach presented here.

2 The Multifield Model

The model equations used in this work are given here. Section 2.1 develops the model equations for the rate of change of mass, linear momentum, and total energy of the interacting materials considered. Section 2.2 shows how the differing frames of reference are reconciled in the FSI approach used here. Section 2.3 discusses one peculiarity of the approach that arises from the practice of using different frames of reference for the fluid and solid materials.

2.1 Model equations

The genesis of the Multifield model is given briefly here, a more thorough version can be found in [?]. The Multifield model is just an ensemble average of the exact conservation equations for a collection of materials, any *one* of which can reside at a point in space time (\mathbf{x}_o, t) . To be general, suppose there are N materials. The state at (\mathbf{x}_o, t) is given by the density, velocity, total energy, stress, and material type indicator $[\rho_o, \mathbf{u}_o, E_o, \boldsymbol{\sigma}_o, \alpha_r]$, $r = 1, 2, \dots, N$. The subscript “o” refers to the value of the quantity at a point in space. For each of the N materials, α_r is Saffman’s \mathcal{H} function[?], defined everywhere in space: it is equal to one if r-material is found at (\mathbf{x}_o, t) , and is zero otherwise. The \mathcal{H} function is just a ledger containing the observer’s record of what material happened to be at (\mathbf{x}_o, t) in any one of the infinite members of the ensemble. The exact evolution equations in conservative differential form with gravitational acceleration \mathbf{g} are

$$\frac{\partial \rho_o}{\partial t} = -\nabla \cdot \rho_o \mathbf{u}_o \quad (1)$$

$$\frac{\partial \rho_o \mathbf{u}_o}{\partial t} = -\nabla \cdot \rho_o \mathbf{u}_o \mathbf{u}_o + \nabla \cdot \boldsymbol{\sigma}_o + \rho_o \mathbf{g} \quad (2)$$

$$\frac{\partial \rho_o E_o}{\partial t} = -\nabla \cdot \rho_o E_o \mathbf{u}_o + \nabla \cdot \boldsymbol{\sigma}_o \cdot \mathbf{u}_o - \nabla \cdot \mathbf{q}_o + \rho_o \mathbf{u}_o \cdot \mathbf{g} \quad (3)$$

These equations are closed by appropriate constitutive models for the stress (or stress rate), equations of state, and the heat flux vector \mathbf{q}_o due to thermal conduction. An exact equation for the evolution of α_r is not available, except when the materials never change identity (that is, no transformations in material type occur, in which case α_r is invariant). For the purposes here we just need to be clear that

$$\frac{\partial \alpha_r}{\partial t} + \mathbf{u}_o \cdot \nabla \alpha_r \equiv \frac{D_o \alpha_r}{Dt}, \quad (4)$$

where we use the subscript o on the material derivative to signify that the material trajectory is \mathbf{u}_o . The equivalence sign is used to emphasize that this is just a definition, not a closure relation. Equation 4 is used as a placeholder for what represents the change in material type due to physical processes (mass exchange between fields).

Let angle brackets signify the ensemble average, which is like an arithmetic average over the ensemble; this is formally an integral over a weighted probability function. The real quantities of interest are the ensemble averaged ones, defined with the help of Saffman's \mathcal{H} function. The data at (\mathbf{x}_o, t) are discontinuous (called weak solutions); application of the ensemble averaging operator creates continuous ones at general locations in space time (\mathbf{x}, t) . The continuous (averaged) variables are referred to as "field" variables. They are

$$\begin{aligned}\rho_r &\equiv \langle \alpha_r \rho_o \rangle : \text{mean r-field total mass density} \\ \rho_r \mathbf{u}_r &\equiv \langle \alpha_r \rho_o \mathbf{u}_o \rangle : \text{mean r-field total momentum density} \\ \rho_r E_r &\equiv \langle \alpha_r \rho_o E_o \rangle : \text{mean r-field total energy density} \\ \theta_r \boldsymbol{\sigma}_r &\equiv \langle \alpha_r \boldsymbol{\sigma}_o \rangle : \text{mean r-field stress} \\ \theta_r &\equiv \langle \alpha_r \rangle : \text{averaged r-field } \mathcal{H} \text{ function}\end{aligned}$$

Evolution equations for the field variables are formally obtained by taking the partial time derivative of the definition, and rearranging with the help of the exact equations. For the mass conservation equation, the result is

$$\frac{\partial \rho_r}{\partial t} + \nabla \cdot \rho_r \mathbf{u}_r = \left\langle \rho_o \frac{D_o \alpha_r}{Dt} \right\rangle$$

which can be integrated over an arbitrary volume of space V

$$\int_V \left(\frac{\partial \rho_r}{\partial t} + \nabla \cdot \rho_r \mathbf{u}_r \right) dV = \int_V \left\langle \rho_o \frac{D_o \alpha_r}{Dt} \right\rangle dV . \quad (5)$$

The left side is the total rate at which r-mass changes in a volume moving with the r-field mean velocity; it is equal to the r-field material derivative of the r-mass $D_r M_r / Dt$ (where the subscript r on the material derivative means that the transport velocity is \mathbf{u}_r). Accordingly, the right side is the total rate at which r-mass is created or destroyed in V due to conversion to/from other material types, while moving along the instantaneous trajectory \mathbf{u}_o . Because any field can contribute/receive mass to/from the r-field, we can express this by a sum over all materials. Let Γ_{rs} be the rate at which r-mass is converted to/from s-mass, averaged in V . Then we can write

$$\frac{D_r M_r}{Dt} = \int_V \left\langle \rho_o \frac{D_o \alpha_r}{Dt} \right\rangle dV = V \sum_{s=1}^N \Gamma_{rs} = V \Gamma_r \quad (6)$$

which signifies the net rate at which r-material is generated (or depleted) in an arbitrary volume, as a result of conversion to/from all other fields. This is the total mass exchange rate, per unit of volume. These steps define a volume average of the ensemble average of the differential equation for the mass.

Using the foregoing notation, we have the (volume & ensemble) averaged equations

$$\frac{1}{V} \frac{D_r M_r}{Dt} = \Gamma_r \quad (7)$$

$$\begin{aligned} \frac{1}{V} \frac{D_r (M_r \mathbf{u}_r)}{Dt} = & - \nabla \cdot \langle \rho_o \alpha_r \mathbf{u}'_r \mathbf{u}'_r \rangle + \theta_r \nabla \cdot \boldsymbol{\sigma} + \nabla \cdot \theta_r (\boldsymbol{\sigma}_r - \boldsymbol{\sigma}) \\ & + \rho_r \mathbf{g} + \sum_{s=1}^N \mathbf{f}_{rs} + \sum_{s=1}^N \mathbf{u}_{rs} \Gamma_{rs} \end{aligned} \quad (8)$$

$$\begin{aligned} \frac{1}{V} \frac{D_r (M_r e_r)}{Dt} = & - \rho_r p \frac{D_r v_r}{Dt} - \nabla \cdot \langle \rho_o \alpha_r e'_r \mathbf{u}'_r \rangle + \theta_r \boldsymbol{\tau}_r : \nabla \mathbf{u}_r - \nabla \cdot \theta_r \mathbf{q}_r \\ & + \rho_r \varepsilon_r + \sum_{s=1}^N h_{sr} + \sum_{s=1}^N (e + pv)_{rs} \Gamma_{rs} \end{aligned} \quad (9)$$

where the right side of each equation is the averaged rate occurring in V . Also, the averaged r-field internal energy comes from $E_r = e_r + \frac{1}{2} u_r^2$; in which e_r typically includes all internal modes (translational + vibrational + rotational + chemical).

Equations 7 - 9 are the averaged model equations for mass, momentum, and internal energy of r-material. The unsubscripted $\boldsymbol{\sigma}$ is the mean mixture stress, taken here to be isotropic, so that $\boldsymbol{\sigma} = -p\mathbf{I}$ in terms of the hydrodynamic pressure p . In this, the deviatoric part of the material stress is given by $\boldsymbol{\tau}_r = \boldsymbol{\sigma}_r - \frac{1}{3} \mathbf{I} \text{Tr}(\boldsymbol{\sigma}_r)$.

In Eq. 8 the quantity $-\langle \rho_o \alpha_r \mathbf{u}'_r \mathbf{u}'_r \rangle$ is the r-material fluctuational momentum flux, otherwise known as the multifield Reynolds Stress. Similarly, in Eq. 9 $-\langle \rho_o \alpha_r e'_r \mathbf{u}'_r \rangle$ is the r-material fluctuational flux of internal energy, while $\rho_r \varepsilon_r$ is the r-material fluctuational dissipation rate. Each of these multiphase turbulence terms, which must be modeled, was neglected in the current work, they are included above for completeness.

In Eq. 8 the term $\sum_{s=1}^N \mathbf{f}_{rs}$ signifies a model for the momentum exchange among materials. This term results from the deviation of the r-field stress from the mean stress, averaged. This is typically modeled as a function of the relative velocity between materials at a point. (For a two material problem this term might look like $\mathbf{f}_{12} = K_{12} \theta_1 \theta_2 (\mathbf{u}_1 - \mathbf{u}_2)$ where the coefficient K_{12} determines the

rate at which momentum is transferred between materials). Likewise, in Eq. 9, $\sum_{s=1}^N h_{sr}$ represents an exchange of heat energy among materials and for a two material problem typically takes the form $h_{12} = H_{12}\theta_1\theta_2(T_2 - T_1)$ where T_r is the r-material temperature and the coefficient H_{rs} is analogous to a convective heat transfer rate coefficient. The heat flux is given by $\mathbf{q}_r = -\rho_r b_r \nabla T_r$ where the kinematic thermal diffusion coefficient b_r is an effective one that contains both molecular and turbulent effects (when the turbulence is included).

In Eqs. 8 and 9, the velocity \mathbf{u}_{rs} and the enthalpy $(e + pv)_{rs}$ are the velocity and enthalpy carried with the material that is converted into that of the r-field, from material that was formerly accounted for in the s-field. For practical purposes these are simply the mean values associated with the field donating its mass to r-field. The rate at which the conversion occurs is given by a model for Γ_{rs} which can be any of the well known forms that satisfy the law of mass action. For a specific example, consider a solid propellant (field-1) converted by burning into a reaction product gas (field-2). Typically $\Gamma_{12} = -C(T_1, p)M_1/V$ where the phenomenological coefficient depends on the propellant temperature and the system pressure. Generally, once burning commences it proceeds until the mass is depleted.

Given appropriate constitutive models for the mass exchange rate, the force density, heat flux, and heat exchange, Eqs. 7-9 are still unclosed (despite ignoring the turbulence effects.) The temperature T_r , specific volume v_r , volume fraction θ_r , and hydrodynamic pressure p are all yet to be specified; these quantities are related to the mass density ρ_r and internal energy e_r by way of equations of state. The four relations for the four quantities (T_r, v_r, θ_r, p) are

$$e_r = e_r(v_r, T_r) \tag{10}$$

$$v_r = v_r(p, T_r) \tag{11}$$

$$\theta_r = \rho_r v_r \tag{12}$$

$$0 = 1 - \sum_{s=1}^N \rho_s v_s \tag{13}$$

Equations 10 and 11 are, respectively, the caloric equation of state and the thermal equation of state. Equation 12 defines the ensemble averaged \mathcal{H} function as the volume fraction, θ and with that definition, Eq. 13 follows. We shall refer to Eq. 13 as the multifield equation of state. The hydrodynamic pressure p is the one value permitting arbitrary masses of the multiple materials to occupy the entirety of the volume V (for this reason it has been called the ‘‘equilibration’’ pressure).

For the present purposes, the final closure relation needed is for the material stress $\boldsymbol{\sigma}_r$. In symbolic form this is

$$\boldsymbol{\sigma}_r = \Phi[\mathbf{F}, \boldsymbol{\sigma}_r, \nabla \mathbf{u}_r, *_r] \quad (14)$$

The operator Φ is the general material response law that may depend on the deformation gradient, the stress itself, the averaged r-material rate of strain and a list of variables indicated by the $*_r$ which may include history variables such as a damage parameter, as well as the rotation of the polar axes relative to the axes in a laboratory frame of reference.

Equations 7-14 form a set of eight equations for the state vector $[M_r, \mathbf{u}_r, e_r, T_r, v_r, \theta_r, \sigma_r, p]$, in any arbitrary volume of space V . The Eulerian Lagrangian approach for large deformation FSI problems requires obtaining approximate solutions to this equation system. To clarify some subtle aspects of the numerical solution method used here, a discussion of the different frames of reference employed is given next.

2.2 Frames of Reference

The averaged field equations displayed in the previous section specify the Lagrangian rate of change for the state of the materials momentarily residing in an arbitrary volume of space. The coordinates of that volume may change with time. The key feature of the FSI approach in this paper is the choice of reference frame on a material by material (field by field) basis. To affect this flexibility a generalized Reynolds Transport Theorem is used [?]. Because of its importance to this work, the theorem is developed here.

Leibnitz's Rule, for the time derivative of the volume integral is

$$\frac{D}{Dt} \int_{V(t)} [q] dV = \int_{V(t)} \left[\frac{\partial q}{\partial t} \right] dV + \int_{S(t)} [\hat{\mathbf{n}} \cdot q \mathbf{u}] dS, \quad (15)$$

where q is a quantity which varies within the volume. The integral of q over the volume is the total of that quantity Q . (For $q = 1$ this is just a kinematic expression for the rate of volume change, along the trajectory \mathbf{u} .) In the multifield case there are N different trajectories associated with the averaged velocity of the N fields in the problem. Let the subscript r designate one of those fields. Leibnitz's Rule for any quantity associated with that field is

$$\frac{D_r}{Dt} \int_{V_r(t)} [q_r] dV = \frac{D_r Q_r}{Dt} = \int_{V_r(t)} \left[\frac{\partial q_r}{\partial t} \right] dV + \int_{S_r(t)} [\hat{\mathbf{n}} \cdot q_r \mathbf{u}_r] dS. \quad (16)$$

Now consider a second volume (that of a computational grid, say), moving with a completely arbitrary velocity \mathbf{u}_g which may be time dependent, time steady, or zero. The corresponding rule, operating again on q_r is

$$\frac{D_g}{Dt} \int_{V_g(t)} [q_r] dV = \frac{D_g Q_r}{Dt} = \int_{V_g(t)} \left[\frac{\partial q_r}{\partial t} \right] dV + \int_{S_g(t)} [\hat{\mathbf{n}} \cdot q_r \mathbf{u}_g] dS. \quad (17)$$

Let us now consider an instant in time at which the surfaces bounding the two volumes is exactly overlapping. At that instant the integrals cover precisely the same space, so we can subtract one from the other thereby eliminating the term involving the partial derivative. That is,

$$\frac{D_g Q_r}{Dt} + \int_{S_g(t)} [\hat{\mathbf{n}} \cdot q_r (\mathbf{u}_r - \mathbf{u}_g)] dS = \frac{D_r Q_r}{Dt}. \quad (18)$$

Using the divergence theorem this can be written

$$\frac{D_g Q_r}{Dt} + V \nabla \cdot q_r (\mathbf{u}_r - \mathbf{u}_g) = \frac{D_r Q_r}{Dt}, \quad (19)$$

in which we implicitly assume that the gradient is constant in the volume V . Equation 19 is the generalized Reynolds Transport Theorem. It relates the change in a total quantity (Q) in a volume moving with velocity \mathbf{u}_g to the rate of change along the material motion \mathbf{u}_r . The difference between the two rates is the second term on the left, called the advection term. Equation 19 is valid, so long as the r-Lagrangian volume and the grid volume are precisely overlapping at the instant for which the evaluation is made.

In the FSI approach used here, $\mathbf{u}_g = \mathbf{u}_r$ for the field representing a solid structure and for the fluid field $\mathbf{u}_g = 0$. Hence we say that the solid field state is integrated in the Lagrangian (material) frame of reference, and the fluid field state is integrated in the Eulerian (laboratory) frame. Thus, the approach uses mixed frames of reference. At the instant the states are to be updated in time, the solid field state is interpolated to the center of each grid volume in the computational domain. In this way, the gradients and state differences that measure the change in state are evaluated in the same volume of space, as is required by Eq. 19.

2.3 Mixed frames of reference

When mixed reference frames are used it becomes necessary to integrate the state relations Eqs. 10-13 in the differential form. The reason for this was

shown in detail by Kashiwa *et al.*[?] by considering the model equations in the incompressible limit. This section illustrates the issue, and its resolution.

Consider the multiphase equation of state for the two field case, and multiply by the grid volume V in which the equation is to be satisfied. Because $\rho_r = M_r/V$ this is

$$0 = V - M_s v_s(p, T_s) - M_f v_f(p, T_f)$$

where the subscripts designate solid and fluid respectively. Now let $v_s =$ constant, which corresponds to an isothermal incompressible material. Let the fluid field be a perfect gas with gas constant R_f , so that $v_f = R_f T_f/p$. The solution for p is

$$p = M_f R_f T_f / (V - M_s v_s)$$

which can always be found, providing that the solid field does not occupy all of the space in V , that is, $M_s v_s < V$. If the field equations for both solid and fluid are integrated in the Eulerian frame, this condition can be guaranteed by a physical stress on the solid field that is compressive (sometimes called a “configuration” stress because the specific volume of the solid is constant). If instead the solid field is integrated in the Lagrangian frame, the mass M_s in V is approximated by interpolation from mass points near V , in which case the condition $M_s v_s < V$ can not be guaranteed in general.

The apparent pathology is removed by using Eqs. 11-13 and the generalized Reynolds Transport Theorem for the r-material specific volume to derive an expression for the specific volume, or volume per unit of mass. The specific volume can be considered to be a dynamic (averaged) variable of the state, to be integrated in time from an initial condition. When this is done, the total volume associated with the materials is

$$V_t = \sum_{r=1}^N M_r v_r$$

so the volume fraction is simply $\theta_r = M_r v_r / V_t$ (which sums to one by definition).

The development of the rate equation of the r-material specific volume is given in the appendix. The final result is:

$$\frac{D_r(M_r v_r)}{Dt} = V \left[v_r \Gamma_r + f_r^\theta \nabla \cdot \mathbf{u} + \theta_r \beta_r \frac{D_r T_r}{Dt} - f_r^\theta \sum_{s=1}^N \theta_s \beta_s \frac{D_s T_s}{Dt} \right]. \quad (20)$$

In the differential limit, the multiphase equation of state is satisfied. However, in the discrete case, characteristic of all numerical approximations, Eq. 13 will not be exactly satisfied, so a correction must be applied. This correction

is discussed in the next section, where the numerical solution algorithm is described. In the limit $\kappa \rightarrow 0$ all materials are incompressible, and Eq. 51 becomes the equation for p whose numerical approximation requires no correction. Hence in the incompressible limit the discrete approximation is once again exact; for compressible materials, we exhibit the goodness of the approximation by way of examples comparing exact and approximate solutions.

3 Solution Algorithm

The foundation of the approach described here is the discretized multifield equations for mixtures of materials as described in Sec. 2.1. These equations are integrated in the Eulerian frame. The numerical algorithm used is described in Sec. 3.1. The algorithm for integrating those fields that are described in the Lagrangian frame (solids) using the Material Point Method is described in Sec. 3.2. The algorithmic details necessary for incorporating the MPM within the Eulerian multifield solution to achieve a tightly coupled “average” multifield interaction capability is provided in Sec. 3.3. This combined algorithm provides a tightly coupled, full physics, fluid structure interaction capability.

3.1 Eulerian multifield method

The Eulerian multifield method implemented here is a cell centered, finite volume, multimaterial version of the ICE (for Implicit, Continuous fluid, Eulerian) method [?] developed by Kashiwa and others at Los Alamos National Laboratory [?]. “Cell centered” means that all elements of the state are colocated at the grid cell center (in contrast to a staggered grid, in which velocity components may be centered at the faces of grid cells, for example). This collocation is particularly important in regions where a material mass is vanishing. By using the same control volume for mass and momentum it can be assured that as the material mass goes to zero, the mass and momentum also go to zero at the same rate, leaving a well defined velocity. The technique is fully compressible, allowing wide generality in the types of problems that can be efficiently computed.

Our use of the cell centered ICE method employs time splitting: first, a Lagrangian step updates the state due to the physics of the conservation laws (i.e., right hand side of Eqs. 7-9); this is followed by an Eulerian step, in which the change due to advection is evaluated. For solution in the Eulerian frame, the method is well developed and described in [?].

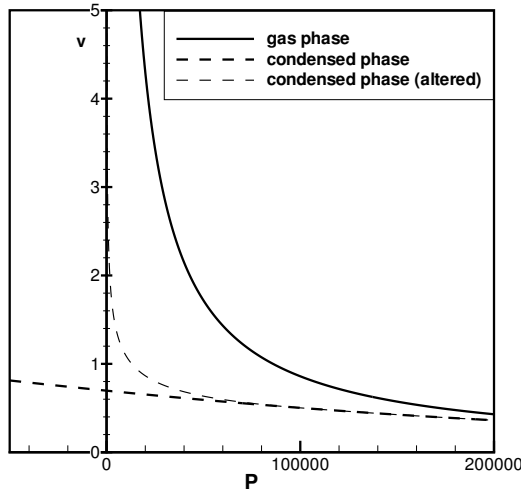


Fig. 1. Specific volume *vs* pressure for a gas phase material and a condensed phase material. Light dashed line reflects an altered condensed phase equation of state to keep all materials in positive equilibration pressure space.

In the mixed frame approach used here, a modification to the multifield equation of state is needed. Equation 13 is unambiguous when all materials are fluids or in cases of a multifield flow consisting of dispersed solid grains in a carrier fluid. However in fluid structure problems the stress state of a submerged structure may be strongly directional, and the isotropic part of the stress has nothing to do with the hydrodynamic (equilibration) pressure p . The equilibrium that typically exists between a fluid and a solid is at the interface between the two materials: there the normal part of the solid stress equals the pressure exerted by the fluid on the solid. Because the orientation of the interface is not explicitly known at any point (it has been averaged away, in effect) such an equilibrium cannot be computed.

The difficulty, and the modification that resolves it, can be understood by considering a solid material in tension coexisting with a gas. For solid materials, the equation of state is just the bulk part of the constitutive response (that is, the isotropic part of the stress versus specific volume and temperature). If one attempts to equate the isotropic part of the stress with the fluid pressure, there exist regions of pressure-volume space for which Eq. 13 has no physical solutions (because the gas pressure is only positive). This can be seen schematically in Fig. 1, which sketches equations of state for a gas phase (solid line) and a condensed phase (heavy dashed line), at an arbitrary temperature. Recall that the isothermal compressibility is the negative slope of the specific volume versus pressure. Imbedded structures considered here are condensed phase and possess a very much smaller compressibility than the gasses in which they are submerged, at low pressure. Nevertheless the variation of condensed phase specific volume can be important at very high

pressures, where the compressibilities of the gas and condensed phase materials can become comparable (as in a detonation wave, for example). Because the speed of shock waves in materials is determined by their equations of state, obtaining accurate high pressure behavior is an important goal of our FSI studies.

To compensate for the lack of directional information for the imbedded surfaces in our problems, we evaluate the condensed phase equations of state in two parts as follows. Above a specified positive threshold pressure, the full equation of state is respected; below that threshold pressure (typically one atmosphere), the condensed phase pressure follows a polynomial chosen to be continuous and smooth at the threshold value and approaches zero as the specific volume becomes large. The effect of this treatment is to decouple the condensed phase specific volume from the stress when the isotropic part of the stress falls below a threshold value. (This is akin to using a configuration stress acting on an incompressible material.) In regions of coexistence at states below the threshold pressure, p tends rapidly toward zero (Fig. 1 light dashed line), and the full material stress dominates the dynamics as it should. An example of just such a situation, with a fluid in compression and a solid in tension is demonstrated in Sec. 4.

3.2 The Material Point Method

A new feature of the approach presented here is the ability to neatly couple a Lagrangian description for selected materials within the overarching multifield method. Specifically, the underlying theory is the multifield equations, solved on an Eulerian mesh. However, materials with solid like behavior and history dependent response laws are more conveniently treated by Lagrangian methods. The unification of the Lagrangian method within the multifield solution is described in Sec. 3.3.

The Lagrangian frame representation adopted here describes the state variables of the material on particles, or “material points.” The specific numerical technique used is known as the Material Point Method (MPM). Originally described by Sulsky, et al., [?,?], the MPM is a particle method for structural mechanics simulations. MPM is an extension to solid mechanics of FLIP [?], which is a particle in cell (PIC) method for fluid flow simulation. The method typically uses a regular structured grid as a computational scratchpad for computing spatial gradients. This same grid also functions as an updated Lagrangian grid that moves with the particles during advection and thus eliminates the diffusion problems associated with advection on an Eulerian grid. At the end of a timestep, the grid is reset to the original regularly ordered position.

In explicit MPM, the equations of motion are cast in the form [?]:

$$\mathbf{M}_g \cdot \mathbf{a}_g = \mathbf{Fext}_g - \mathbf{Fint}_g \quad (21)$$

where \mathbf{M}_g is the mass matrix, \mathbf{a}_g is the acceleration vector, \mathbf{Fext}_g is the external force vector (sum of the body forces and tractions), and \mathbf{Fint}_g is the internal force vector resulting from the divergence of the material stresses. Throughout this section, variables subscripted with a g indicate quantities that exist on the nodes of computational grid, while variables subscripted with a p are particle based. In this development we will only be considering a single material. An extension describing contact between multiple materials is given by [?].

The solution procedure begins by interpolating the particle state to the grid, to form \mathbf{M}_g , \mathbf{Fext}_g , and to determine a velocity on the grid \mathbf{v}_g . In practice, a lumped mass matrix is usually used. These quantities are calculated by the following equations, where the \sum_p represents a summation over all particles:

$$\mathbf{M}_i = \sum_p S_{ip} m_p, \quad \mathbf{v}_i = \frac{\sum_p S_{ip} m_p \mathbf{v}_p}{\mathbf{M}_i}, \quad \mathbf{Fext}_i = \sum_p S_{ip} \mathbf{Fext}_p \quad (22)$$

where i refers to individual nodes of the grid. m_p is the particle mass, \mathbf{v}_p is the particle velocity, and \mathbf{Fext}_p is the external force on the particle. S_{ip} is the i th node's shape function evaluated at \mathbf{x}_p , the position of the p th particle. Traditionally, standard trilinear shape functions are employed, but recently higher order interpolants, as described in [?], have yielded improved results.

At this point, a velocity gradient, $\nabla \mathbf{v}_p$ is computed at the particle using the velocities interpolated to the grid:

$$\nabla \mathbf{v}_p = \sum_p \mathbf{G}_{ip} \mathbf{v}_i \quad (23)$$

where \mathbf{G}_{ip} is the gradient of the i th nodes shape function, evaluated at \mathbf{x}_p .

This is used as input to a constitutive model which is evaluated on a per particle basis, the result of which is the Cauchy stress at each particle, $\boldsymbol{\sigma}_p$. With this, the internal force due to the divergence of the stress is calculated via:

$$\mathbf{Fint}_i = \sum_p \mathbf{G}_{ip} \boldsymbol{\sigma}_p V_p, \quad (24)$$

where V_p is the particle volume.

Equation 21 can then be solved for \mathbf{a}_g . An explicit backward Euler method is used for the time integration:

$$\mathbf{v}_i^L = \mathbf{v}_i + \mathbf{a}_i dt \quad (25)$$

and the particle position and velocity are explicitly updated by:

$$\mathbf{v}_p(t + dt) = \mathbf{v}_p(t) + \sum_i S_{ip} \mathbf{a}_i dt \quad (26)$$

$$\mathbf{x}_p(t + dt) = \mathbf{x}_p(t) + \sum_i S_{ip} \mathbf{v}_i^L dt \quad (27)$$

This completes one timestep.

As described here, MPM is able to function independently as a method for performing structural mechanics simulations, and it has many important applications and unique capabilities in this area. Furthermore, by describing and implementing it in an independent fashion, validation of the method itself as well as submodels (e.g., constitutive models and contact) is simplified. However, we emphasize that its use here is for selected material field description within the general multifield formulation. This integration is described next.

3.3 Integration of the Material Point Method within the Eulerian multifield ICE Formulation

The key feature of this work is the development, demonstration, and validation of a tightly coupled, multifield “averaged” solution approach that allows simulations of an arbitrary number of materials undergoing a variety of physical and chemical processes. Fundamental to the proposed approach is the representation of a material field in either an Eulerian or Lagrangian reference frame, integrated within a general multifield description. This allows treating specific phases in their traditionally preferred frame of reference, Lagrangian for solid, Eulerian for fluid. The MPM algorithm, described in the previous section, is used to time advance those materials that are best described in a Lagrangian reference frame. However, by choosing the background mesh used to update the MPM materials, to be the same mesh used in the multi-material Eulerian description, all interactions among materials can be enforced to occur in the common framework. This results in a robust and tightly coupled solution for interacting materials with very different response behaviors.

All materials, solid or fluid, will have a presence in the Eulerian multifield description. This common reference frame is used for all physics that involve

mass, momentum, or energy exchange among materials. This allows for a tight coupling between the fluid and solid phases. *The coupling occurs directly within the terms in the multifield equations.* Since a common Eulerian frame of reference is used for interactions among materials, typical problems with convergence and stability of solutions for separate domains communicating only through boundary conditions are alleviated. Thus, all solid phase materials thus have a dual representation - in both the Lagrangian (MPM) and Eulerian framework.

The principal difference between solid and fluid materials is characterized by their response to deformation, as represented by equations of state and constitutive models. As such, it is primarily in advection and in the computation of internal forces that the use of the separate reference frames becomes important. Eulerian advection is typically subject to significant diffusion. Therefore if the Eulerian frame is used exclusively for both solid and fluid materials, the interface between the materials will become smeared and nonphysical behavior may result. The use of a particle description for the solid advection eliminates this problem. Furthermore, while straining history does not typically play a role in the stress field in a fluid, it is important in many engineering solid materials to describe phenomenon such as plasticity. The particle description of the solid provides a convenient frame to evaluate the solid material stress, and to store and carry forward in time the relevant history variables. This role of the particle is similar to the role that Gaussian integration points play in the finite element method. On the other hand, if a particle description is used for fluid phases, the random behavior of fluid motion may result in particle distributions that are at best suboptimal and at worst insufficient to achieve a solution. This limits the utility of the MPM for fluid calculations. However, the integration of the two, where part of the calculation takes place in a common reference frame, allows each material phase to enjoy it's optimum description and achieves a tight coupling.

To illustrate how this coupling is accomplished in an algorithmic fashion the explicit steps for advancing a fluid-solid problem from time t to time $t + \Delta t$ are described below.

- (1) **Interpolate particle state to grid:** A simulation timestep begins by interpolating the particle description of the solid to the grid, so that all materials are described in a common frame of reference. This starts with an interpolation of particle data to grid vertices, or nodes, as described in Eq. 22, and is followed by a subsequent interpolation from the nodes to the cell centers. Since our work uses a uniform structured grid, each node has equal weight in its contribution to the cell centered value. The exception to this is near computational boundaries. For instance, if symmetric boundary conditions are used, the weight of those nodes on the boundary must be doubled in order to achieve the desired effect.

- (2) **Compute the equilibrium pressure:** While Eq. 13 and the surrounding discussion describes the basic process, a few specifics warrant further explanation. In particular, the manner in which each material's volume fraction is computed is crucial. Typically, in multi-material CFD calculations, this would simply be the material volume divided by the cell volume. However, because the solid and fluid materials are advected in different manners (see below) the total volume of material in a cell is not necessarily equal to the volume of a computational cell. Because of this, it is important to have an accurate accounting of the volume of material in each cell. This is done by solving the evolution equation for each material's specific volume given by Eq. 53 and described below in step 11.

With the materials' masses and specific volumes in hand, material volume can be computed and summed to find the total material volume. The volume fraction θ_r is then computed as the volume of r-material per total material volume. With this, the solution of Eq. 13 can be carried out at each cell using a Newton-Raphson technique[?], which results in new values for the equilibrium pressure, p_{eq} , volume fraction, θ_r and specific volume, v_r .

- (3) **Compute face centered velocities, u_r^* , for the Eulerian advection:** At this point, fluxing velocities are computed at each cell face. The expression for this is based on a time advanced estimate for the cell centered velocity. A full development can be found in [?] and [?] but here, we only state the result:

$$u_r^* = \frac{\rho_{rL}u_{rL} + \rho_{rR}u_{rR}}{\rho_{rL} + \rho_{rR}} - \left(\frac{2v_{rL}v_{rR}\Delta t}{v_{rL} + v_{rR}} \right) \left(\frac{p_{eqR} - p_{eqL}}{\Delta x} \right) \quad (28)$$

The first term above is a mass weighted average of the logically left and right cell centered velocities and the second term is a pressure gradient acceleration term. Not shown explicitly here is the necessary momentum exchange at the face centers. This is done here in the same manner as it is described subsequently in step 10 for the cell centered momentum exchange.

- (4) **Multiphase chemistry:** Compute sources of mass, momentum, energy and specific volume as a result of phase changing chemical reactions for each r-material, Γ_r , $u_r\Gamma_r$, $e_r\Gamma_r$ and $v_r\Gamma_r$. Specifics of this step are model dependent, but in general the most important consideration is to accurately account for the changes in state for all materials involved, particularly the reactant material. Failure to do so can result in unreasonable values for temperature and velocity as the mass of the reactant material is consumed. When the reactant material is described by particles, this is somewhat simplified as decrementing the particle

mass automatically decreases the momentum and internal energy of that particle by the appropriate amount. Otherwise, care must be taken to reduce the momentum and internal energy of the reactant by amounts proportional to the mass consumed each timestep. This mass, momentum and internal energy is transferred to the product material's state.

- (5) **Compute an estimate of the time advanced pressure, p :** Based on the volume of material being added to (or subtracted from) a cell in a given timestep, an increment to the cell centered pressure is computed using:

$$\Delta p = \Delta t \frac{\sum_{r=1}^N v_r \Gamma_r - \sum_{r=1}^N \nabla \cdot (\theta u^*)_r}{\sum_{r=1}^N (\theta \kappa)_r} \quad (29)$$

$$p = p_{eq} + \Delta p \quad (30)$$

where κ^r is the r-material bulk compressibility. The first term in the numerator of Eq. 29 represents the change in volume due to reaction, i.e., a given amount of mass would tend to occupy more volume in the gas phase than the solid phase, leading to an increase in pressure. The second term in the numerator represents the net change in volume of material in a cell due to flow into or out of the cell. The denominator is essentially the mean compressibility of the mixture of materials within that cell. (Note that in simulations involving phase change, improved accuracy may be achieved by adjusting the volume fractions in Eq. 29 to account for the accompanying change in each material's volume.) This increment in pressure is added to the equilibrium pressure computed in step 2 and is the pressure used for the remainder of the current timestep. Again, the details leading to this equation can be found in [?].

- (6) **Face Centered Pressure p^* :** The calculation of p^* is discussed at length in [?]. For this work, it is computed using the updated pressure by:

$$p^* = \left(\frac{p_L}{\rho_L} + \frac{p_R}{\rho_R} \right) / \left(\frac{1}{\rho_L} + \frac{1}{\rho_R} \right) \quad (31)$$

where the subscripts L and R refer to the logically left and right cell centered values respectively, and ρ is the sum of all material's densities in that cell. This will be used subsequently for the computation of the pressure gradient, ∇p^* .

- (7) **Material Stresses:** For the solid, we calculate the velocity gradient at each particle based on the grid velocity (Eq. 23) for use in a constitutive

model to compute particle stress. Fluid stresses are computed on cell faces based on cell centered velocities.

- (8) **Accumulate sources of mass, momentum and energy at cell centers:** These terms are of the form:

$$\Delta(m)_r = \Delta t V \sum_{s=1, s \neq r}^N \Gamma_s \quad (32)$$

$$\Delta(mu)_r = -\Delta t V \left[\theta_r \nabla p^* + \nabla \cdot \theta_r (\boldsymbol{\sigma}_r - \boldsymbol{\sigma}) + \sum_{s=1, s \neq r}^N u_s \Gamma_s \right] \quad (33)$$

$$\Delta(me)_r = -\Delta t V \left[f_r^\theta p \sum_{s=1}^N \nabla \cdot (\theta u^*)_s + \sum_{s=1, s \neq r}^N e_s \Gamma_s \right] \quad (34)$$

where f_r^θ is a measure of the relative compressibility of the r-material in a cell as in Eq. ???. Note that the only source of internal energy being considered here is that due to “flow work”. This is required for the compressible flow formulation, but other terms, such as heat conduction are at times included.

- (9) **Compute Lagrangian phase quantities at cell centers:** The increments in mass, momentum and energy computed above are added to their time t counterparts to get the Lagrangian values for these quantities. Note that here, some Lagrangian quantities are denoted by an L -superscript. This indicates that all physical processes have been accounted for except for momentum and heat exchange which is described in the following step.

$$(m)_r^L = (m)_r^t + \Delta(m)_r \quad (35)$$

$$(mu)_r^{L-} = (mu)_r^t + \Delta(mu)_r \quad (36)$$

$$(me)_r^{L-} = (me)_r^t + \Delta(me)_r \quad (37)$$

- (10) **Momentum and heat exchange:** The last step in the Lagrangian phase is the exchange of momentum and heat between materials.

$$(mu)_r^L = (mu)_r^{L-} + \Delta t m_r \sum_{s=1}^N \theta_r \theta_s K_{rs} (u_s^L - u_r^L) \quad (38)$$

$$(me)_r^L = (me)_r^{L-} + \Delta t m_r c_{v_r} \sum_{s=1}^N \theta_r \theta_s R_{rs} (T_s^L - T_r^L) \quad (39)$$

These equations are solved in a pointwise implicit manner that allows arbitrarily large momentum transfer to take place between materials. Typically, in FSI solutions, very large (10^{15}) values of K are used, which

results in driving contacting materials to the same velocity. Intermaterial heat exchange is usually modeled at a lower rate. Again, note that the same operation must be done following Step 3 above when computing the face centered velocities.

- (11) **Specific volume evolution:** As discussed above in step 2, in order to correctly compute the equilibrium pressure and volume fraction, it is necessary to keep an accurate accounting of the specific volume for each material. Here, we compute the evolution in specific volume due to the changes in temperature and pressure, as well as phase change, during the foregoing Lagrangian portion of the calculation, according to:

$$\Delta(mv)_r = \Delta t V \left[v_r \Gamma_r + f_r^\theta \nabla \cdot \sum_{s=1}^N \theta_s^* u_s^* + \theta_r \beta_r \dot{T}_r - f_r^\theta \sum_{s=1}^N \theta_s \beta_s \dot{T}_s \right] \quad (40)$$

$$(mv)_r^L = (mv)_r^n + \Delta(mv)_r \quad (41)$$

where β is the constant pressure thermal expansivity and $\dot{T} = \frac{T^L - T^t}{\Delta t}$ is the rate of change of each material’s temperature during the Lagrangian phase of the computation.

- (12) **Advect Fluids:** For the fluid phase, use a suitable advection scheme, such as that described in [?], to move fluid material between cells. This includes the transport of mass, momentum, internal energy and specific volume. As this last item is an intensive quantity, it is converted to material volume for advection, and then reconstituted as specific volume for use in the subsequent timestep’s equilibrium pressure calculation.
- (13) **Advect Solids:** For the solid phase, interpolate the time advanced grid velocity and the corresponding velocity increment back to the particles, and use these to advance the particle’s position and velocity, respectively. This constitutes advection of the solid phase material.

This completes one timestep. In the preceding, the user has a number of options in the implementation. The approach taken here was to develop a working MPM code and a separate working multifield ICE code. We note, however, that the fluid structure interaction methodology should not be looked at in the context of a “marriage” between an Eulerian CFD code and the MPM. The underlying theory is a multifield description that has the flexibility to incorporate different numerical descriptions for solid and fluid fields within the overarching solution process. To have flexibility in treating a widest range of problems, it was our desire that in the coupling of the two algorithms, each of the original codes be able to function independently, or in concert.

Thus, for instance, in step 8 above, for the solid material we’ve chosen not to aggregate all of the momentum sources at the cell centers. Rather, the pressure gradient and mean pressure are computed at the cell centers, and interpolated

back to the nodes, where the integration of the MPM equations normally take place. The time advanced solid material momentum is then aggregated at the cell centers for momentum exchange, and the resulting change in momentum is propagated back to the nodes and eventually to the particles. Also, as described here, this method is fully explicit in time. To make this implicit with respect to the propagation of pressure waves, a Poisson equation is solved in the calculation of Δp , which is in turn used to iteratively update the face centered velocities. This is described in [?].

4 Validation Tests

Because of the complex nature of most interesting fluid structure interaction scenarios, it is difficult to construct tests for the purposes of validation which encompass the entire range of possible behavior of the different phases. The strategy followed here is to validate particular types of behavior, each of which is dominated by a specific part of the coupled governing equations. Still, even for these simple tests, most, if not all, of the terms in those equations must be implemented properly to achieve an accurate solution. Three such tests are presented below.

4.1 Stress Distribution in a Pressurized Cylinder

To demonstrate the ability of the approach to accurately represent the interaction between fluids and solids, a cylinder of finite thickness is pressurized internally and the subsequent stress distribution in the cylinder is presented. The configuration is shown in Fig. 2. A uniform mesh is used and the solid cylinder is represented by material points as shown. The cylinder is made of steel with bulk and shear modulus of 117.0 GPa and 43.8 GPa respectively. Density is 8900 kg/m^3 . Inner radius, r_i , is 0.5 m and outer radius, r_o , is 1.0 m . Although code capabilities are fully three dimensional, this example is two dimensional, with plane strain being the out of plane condition. As shown in Fig. 2 a one-quarter symmetric section of the cylinder was simulated. The fluid is defined everywhere on the mesh, although the volume fraction of the fluid is set to zero in the region occupied by the solid. Pressurization of the cylinder is achieved by adding internal energy to the fluid inside the cylinder over the course of 500 timesteps. The final pressure of 19.4 MPa inside the cylinder then remains constant and viscous damping is used in the solid phase to achieve a quasistatic solution. Because there is very little movement of the materials, this simulation is an especially good test of the transmission of the pressure gradient between the gas and solid at the material interface.

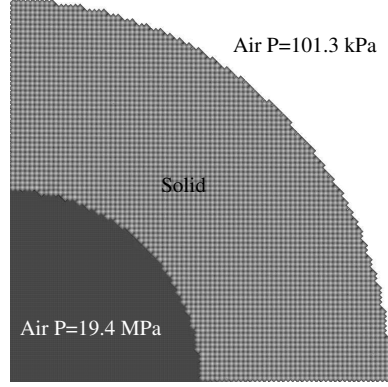


Fig. 2. Initial configuration for pressurization of an annulus. The cylinder is described by material points on the Eulerian mesh of the multi-material solution.

The exact solutions for the radial and circumferential stresses are given by [?] (where P is the pressure inside the container):

$$\sigma_{radial} = \frac{Pr_i^2}{(r_o^2 - r_i^2)} \left(1 - \frac{r_o^2}{r^2} \right) \quad \sigma_{\theta} = \frac{Pr_i^2}{(r_o^2 - r_i^2)} \left(1 + \frac{r_o^2}{r^2} \right) \quad (42)$$

The predicted stress distributions, computed using a grid spacing of 0.025 m in each direction, are compared to the exact solution in Fig. 3a. The agreement is seen to be very good. It is particularly noteworthy that in the solution, there is no explicit representation of a surface or explicit description of surface tractions on the material points describing the cylinder. Coupling occurs completely through the multifield equations (Eq. 8).

This simulation was carried out at several grid resolutions in order to characterize the order of accuracy of this implementation. The error for each resolution was computed by:

$$Error = \frac{1}{N} \sum_N \frac{||\sigma_r + \sigma_{\theta}| - \frac{2}{3}P|}{\frac{2}{3}P} \quad (43)$$

Results from that are shown in Fig. 3b. When plotted in this log-linear manner, the slope of the straight line that best approximates these points indicates the order of accuracy. Here, a slope of 0.89 is found.

4.2 Adiabatic compression of a confined gas by a piston

A one-dimensional simulation of a piston adiabatically compressing a confined gamma-law gas was carried out to test different aspects of the coupled

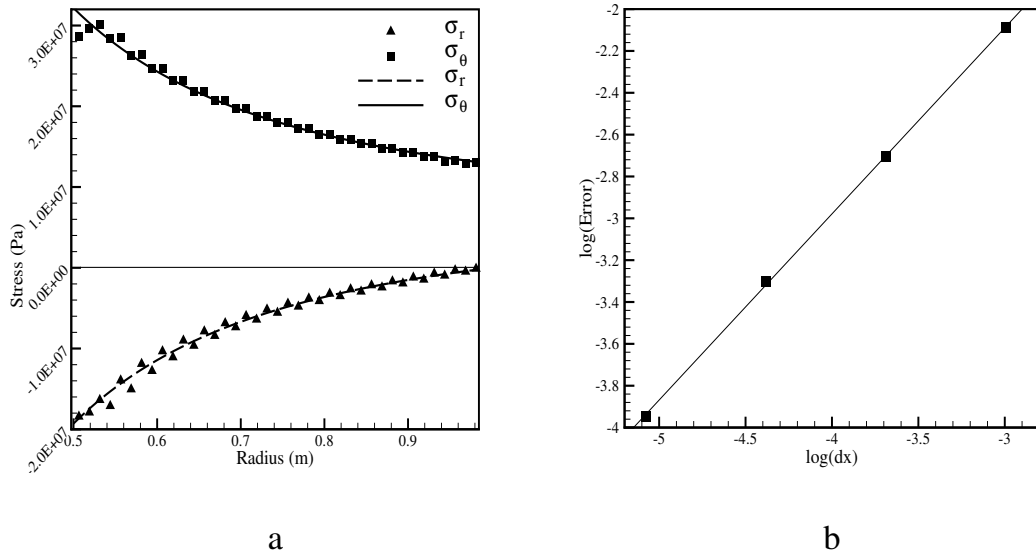


Fig. 3. Results from pressurization of an annulus, (a) radial and circumferential stresses, compared to the theoretical solutions, of the row of particles nearest the x-axis, and (b) natural log of solution error, averaged over all particles, vs. natural log of grid spacing. The slope of the line fit to the four data points indicates an order of accuracy of 0.89.

governing equations. Specifically, this test exercises the Eulerian evolution equation for the specific volume, Eq. 53, the source of internal energy under large volume changes as well as advection. Both are crucial in order to accurately predict the pressure of the confined gas. This simulation also demonstrates that the algorithm accurately describes the interaction between the piston and the gas via momentum coupling as the piston moves slowly through a large number of computational cells. The rigid piston was described by material points and its motion was specified. Figure 4 shows the cell centered gas pressure at the bottom of the cylinder versus time as well as the analytical solution (assuming thermodynamic equilibrium) given by:

$$P_2 = P_1 \left(\frac{V_1}{V_2} \right)^\gamma \quad (44)$$

A large momentum exchange coefficient, ($K_{rs} = 10^{15}$) was chosen. This drives the velocity of the gas and the piston to the same value in cells where both gas and piston are present (i.e., at the interface between the gas and the solid). This enforces a no-slip, no-interpenetration condition between the piston and the gas. For this simulation, the compression ratio of the gas (initial volume/final volume) reached a maximum of 5.9.

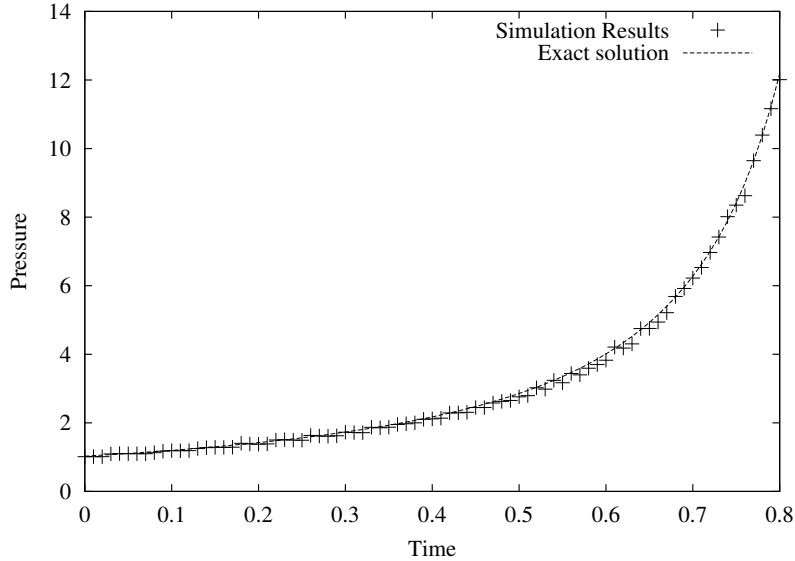


Fig. 4. Adiabatic compression of a confined gas by a piston. Pressure versus time at $y = 0.0$.

4.3 *Supersonic Wedge*

The final validation test presented here is a symmetric 20° wedge moving at Mach 3 through initially stationary air. The main purpose of this test is to demonstrate the ability of the compressible multifield ICE formulation to capture the oblique shocks and expansion fan that result from the interaction of the solid wedge with the surrounding air. Traditionally, tests such as this are done by keeping the geometry fixed and describing it as a boundary condition to a CFD code which moves the fluid over the stationary item.

Figure 5 depicts the wedge, represented by material points, as well as contours of the cell centered pressure on the Eulerian grid. The bold dashed line starting at the leading point of the wedge represents the expected angle of the oblique shock, 38° for ideal inviscid supersonic flow [?] (pp. 308-309). The expansion fan over the top of the wedge and the second shock at the trailing edge of the wedge are also evident as expected. In general, quite good agreement is achieved relative to the anticipated solution. The curvature of the shock away from the body is expected for non ideal supersonic flow.

In addition to the shock capturing, this test also demonstrates another important capability. While the wedge used here is a simple shape, arbitrarily complex geometries can be generated using particle distributions, and their interaction with the surrounding flow field studied, all without the time consuming step of complex mesh generation. The motion of the solid object can be either prescribed or the full dynamic response of the solid can be computed

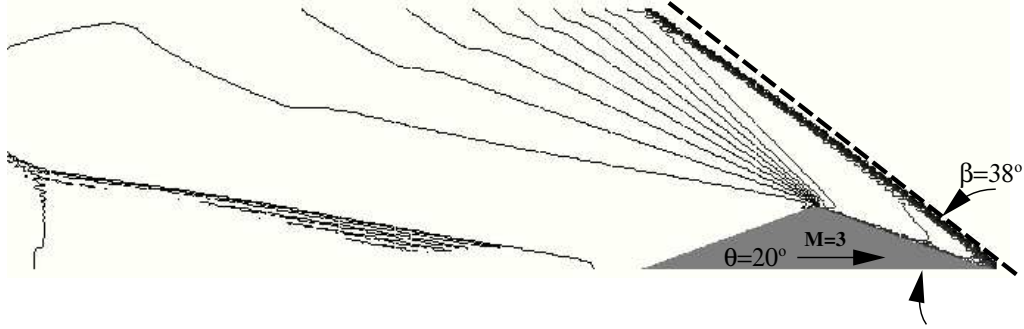


Fig. 5. Wedge moving at Mach 3 through initially stationary air. Contours of pressure are shown.

as it interacts with the flow field. We believe that these are capabilities unique to this approach.

5 Explosion of a Confined Energetic Material

The final simulation illustrates the algorithm’s capabilities with regards to large deformations and the treatment of multiple materials, including intermaterial mass exchange and the interaction of gases from initially separate regions. The simulation configuration is a $1/8^{th}$ symmetric section of a cylindrical steel container filled with a plastic bonded explosive (PBX). A lengthwise notch has been removed from the container to introduce a region of weakness, as shown in Fig. 6a, where the outside of the container is depicted by an isosurface of the steel’s mass. The initial temperature of the container was $650K$, well above the reaction threshold temperature for PBX. The reaction model used allows burning only on the surface of the PBX and is of the form $\Gamma = AKP^n$, where A is the surface area, K is a rate constant and P is the pressure. From the start of the simulation, the PBX begins burning at the interface between itself and the container. Figures 6b-d show the evolution of the container, including its failure, which begins at the notch as expected. As the container fails, product gases resulting from the reaction, depicted by an isosurface of the volume fraction, are seen escaping the failed region. These subsequently expand and mix with the air surrounding the container. In Fig. 6d both the container and the product gases can be seen colliding with the boundaries of the computational domain.

A few features of this simulation warrant further explanation. Initially the volume fraction of the gas was zero within the container. As the reaction proceeded, gas was generated in regions formerly occupied by the solid materials. Next, upon the rupture of the container, product gas from inside the container escapes and interacts with the surrounding air. Both the phase change and the subsequent interaction of gases from initially separate

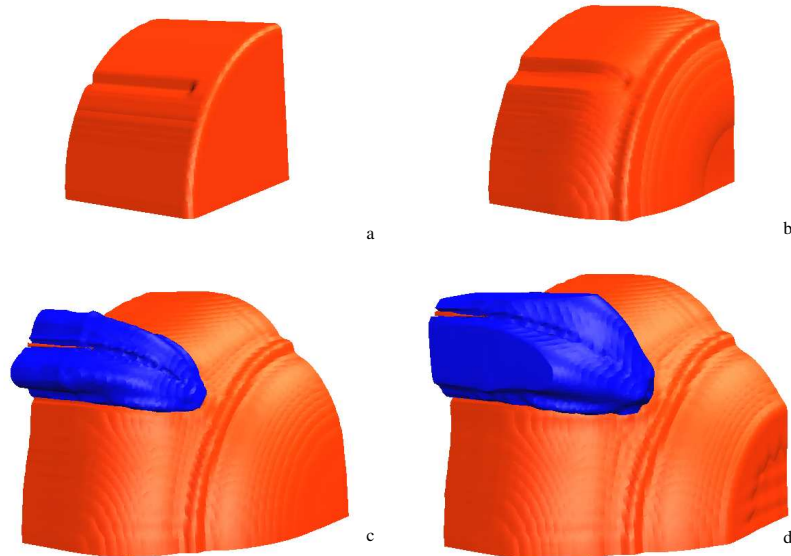


Fig. 6. Deformation and rupture of a steel container pressurized by the reaction of explosive contents. As the container ruptures, product gases of the reaction can be seen escaping the container.

regions are extremely problematic for FSI techniques based on the separated model approach. Finally, in this case, to achieve “failure” of the container, a deficiency in the MPM algorithm was exploited. Namely, when particles are subject to sufficient strain that initially adjacent particles become separated by an entire computational cell, the material no longer behaves as a continuum in this region, and is effectively broken. While this feature was exploited here for demonstration purposes, recently a collaborator has implemented constitutive models in which material failure is determined based on deterministic criteria, including strain rate, shear banding and dislocation. Discussion of these models is beyond the intended scope of this manuscript, and as such these models were not used in its preparation.

6 Discussion and Conclusions

A novel technique for simulation of large deformation Fluid Structure Interaction (FSI) phenomena has been presented. This approach is based upon solving the multifield governing equations for both the solid and fluid materials on an Eulerian mesh. In addition, solid materials have a second representation in the Lagrangian frame in the form of a particle representation, based on the Material Point Method (MPM). This dual representation allows both material phases the advantage of operating within their traditionally preferred frame of

reference, thus alleviating some of the problems typically encountered when attempting to treat both phases in a single reference frame. Several simple validation tests were performed, each of which was intended to bring a degree of confidence to one or more elements of the physics involved in multifield problems. Finally, an example simulation was presented to demonstrate the complex types of problems that this method is capable of treating.

A few words on the applicability of this methodology are appropriate. Currently, the version of the MPM that is described here uses explicit time integration. Typical engineering solids have a large sound speed, and as such, stability considerations require the use of small timesteps. Thus the technique described here is best suited for high rate simulations, such as explosions, detonations, blast wave or projectile interactions, and other scenarios where the timescales involved lend themselves to being treated by explicit integration in time. In cases where one does not need to resolve the dynamic response of the solid, as in the supersonic wedge case of Sec. 4.3, only slight modification is required to allow one to ignore the stability constraint imposed by the solid material. In addition, future plans include incorporating a version of the MPM that uses implicit time integration, such as that described in [?]. This will greatly expand the range of timescales over which the techniques described here is applicable.

7 Appendix: Derivation of the Specific Volume Evolution Equation

The generalized Reynolds Transport Theorem for the r-material specific volume is

$$\begin{aligned} \frac{D_r(M_r v_r)}{Dt} &= v_r \frac{D_r M_r}{Dt} + M_r \frac{D_r v_r}{Dt} \\ &= v_r V \Gamma_r + M_r \frac{D_r v_r}{Dt} \end{aligned} \quad (45)$$

The Lagrangian rate for the change of v_r is obtained by differentiation of the state equation, Eq. 11. That is

$$\frac{D_r v_r}{Dt} = v_r \left(-\kappa_r \frac{D_r p}{Dt} + \beta_r \frac{D_r T_r}{Dt} \right) \quad (46)$$

where the partial derivatives are

$$\kappa_r = - \left[\frac{1}{v_r} \frac{\partial v_r}{\partial p} \right]_T \quad \text{isothermal compressibility ;} \quad (47)$$

$$\beta_r = \left[\frac{1}{v_r} \frac{\partial v_r}{\partial T} \right]_p \quad \text{constant pressure volumetric expansivity .} \quad (48)$$

In the problems shown here, ideal materials with constant specific heats are assumed.

The rate equation for the hydrodynamic pressure begins with the differentiation of the multifield equation of state, Eq. 13, and proceeds with the use of conservation of mass, the definition of the material derivative of v_s , the product rule and Eqs. 46 and 12.

$$\begin{aligned} \frac{\partial}{\partial t} \left[1 - \sum_{s=1}^N (\rho_s v_s) \right] &= 0 = \sum_{s=1}^N \left[\rho_s \frac{\partial v_s}{\partial t} + v_s \frac{\partial \rho_s}{\partial t} \right] \\ &= \sum_{s=1}^N \left[\rho_s \frac{\partial v_s}{\partial t} - v_s \nabla \cdot (\rho_s \mathbf{u}_s) + v_s \Gamma_s \right] \\ &= \sum_{s=1}^N \left[\rho_s \frac{D_s v_s}{Dt} - \rho_s \mathbf{u}_s \cdot \nabla v_s - v_s \nabla \cdot (\rho_s \mathbf{u}_s) + v_s \Gamma_s \right] \\ &= \sum_{s=1}^N \left[\rho_s \frac{D_s v_s}{Dt} - \nabla \cdot (\rho_s \mathbf{u}_s v_s) + v_s \Gamma_s \right] \\ &= \sum_{s=1}^N \left[\theta_s \left(-\kappa_s \frac{D_s p}{Dt} + \beta_s \frac{D_s T_s}{Dt} \right) \right] - \nabla \cdot \sum_{s=1}^N \theta_s \mathbf{u}_s + \sum_{s=1}^N v_s \Gamma_s \end{aligned}$$

At this point it is useful to introduce a few relationships, namely:

$$\kappa = \sum_{s=1}^N \theta_s \kappa_s , \quad (49)$$

$$\mathbf{u} = \sum_{s=1}^N \theta_s \mathbf{u}_s . \quad (50)$$

Use of each of these results in

$$\kappa \frac{D_p p}{Dt} = -\nabla \cdot \mathbf{u} + \sum_{s=1}^N \left(\theta_s \beta_s \frac{D_s T_s}{Dt} \right) \quad (51)$$

where $D_p p / Dt = \partial p / \partial t + \mathbf{u}_p \cdot \nabla p$ in which the transport velocity is

$$\mathbf{u}_p = (\sum_{s=1}^N \theta_s \kappa_s \mathbf{u}_s) / \kappa .$$

However, what we need to complete Eq. 46 is $D_p p / Dt = \partial p / \partial t + \mathbf{u}_p \cdot \nabla p$. To find this, we consider the difference:

$$\begin{aligned}
\kappa \frac{D_r p}{Dt} - \kappa \frac{D_p p}{Dt} &= \left[\kappa \frac{\partial p}{\partial t} + \kappa \mathbf{u}_r \cdot \nabla p \right] - \left[\kappa \frac{\partial p}{\partial t} + \sum_{s=1}^N \theta_s \kappa_s \mathbf{u}_s \cdot \nabla p \right] \\
&= \mathbf{u}_r \sum_{s=1}^N \theta_s \kappa_s \cdot \nabla p - \sum_{s=1}^N \theta_s \kappa_s \mathbf{u}_s \cdot \nabla p \\
&= \kappa (\mathbf{u}_r - \mathbf{u}_p) \cdot \nabla p
\end{aligned}$$

or:

$$\frac{D_r p}{Dt} = \frac{D_p p}{Dt} + (\mathbf{u}_r - \mathbf{u}_p) \cdot \nabla p \quad (52)$$

Substitution of Eq. 52 into Eq. 46 gives a rate equation for the specific volume of the r-material:

$$\begin{aligned}
\frac{M_r}{V} \frac{D_r v_r}{Dt} &= f_r^\theta \nabla \cdot \mathbf{u} + \left(\theta_r \beta_r \frac{D_r T_r}{Dt} - f_r^\theta \sum_{s=1}^N \theta_s \beta_s \frac{D_s T_s}{Dt} \right) \\
&\quad - f_r^\theta \sum_{s=1}^N v_s \Gamma_s - \kappa_r \theta_r (\mathbf{u}_r - \mathbf{u}_p) \cdot \nabla p
\end{aligned} \quad (53)$$

where $f_r^\theta = \theta_r \kappa_r / \kappa$. Finally, Eq. 53 is used with Eq. 45 to give a rate equation for the volume of r-material

$$\begin{aligned}
\frac{1}{V} \frac{D_r (M_r v_r)}{Dt} &= f_r^\theta \nabla \cdot \mathbf{u} + \left(\theta_r \beta_r \frac{D_r T_r}{Dt} - f_r^\theta \sum_{s=1}^N \theta_s \beta_s \frac{D_s T_s}{Dt} \right) \\
&\quad + \left(v_r \Gamma_r - f_r^\theta \sum_{s=1}^N v_s \Gamma_s \right) \\
&\quad - \theta_r \kappa_r (\mathbf{u}_r - \mathbf{u}_p) \cdot \nabla p
\end{aligned} \quad (54)$$

Acknowledgements

This work was supported by the National Science Foundation's Information Technology Research Program under grant CTS0218574, and the U.S. Department of Energy through the Center for the Simulation of Accidental Fires and Explosions, under grant W-7405-ENG-48. Los Alamos National Laboratory is operated by the University of California for the United States Department of Energy under contract W-7405-ENG-36; partial support from the Procter & Gamble Company, and from other DOE programs, is gratefully acknowledged.

References

- [1] M. Lewis, B. Kashiwa, R. Meier, S. Bishop, Nonlinear dynamic fluid-structure interaction calculations with coupled finite element and finite volume schemes, in: ASME Winter Annual Meeting, Chicago, IL, 1994.
- [2] M. Bhardwaj, R. Kapania, E. Reichenbach, G. Guruswamy, Computational fluid dynamics/computational structural dynamics interaction methodology for aircraft wings, *AIAA Journal* 36 (1998) 2179–2186.
- [3] R. Benney, K. Stein, Computational fluid-structure interaction model for parachute inflation, *Journal of Aircraft* 33 (1996) 730–736.
- [4] S. Rugonyi, K. Bathe, On finite element analysis of fluid flows fully coupled with structural interactions, *CMES* 2 (2001) 195–212.
- [5] K. Bathe, H. Zhang, S. Ji, Finite element analysis of fluid flows coupled with structural interactions, *Computers & Structures* 72 (1999) 1–16.
- [6] S. Soo, *Fluid Dynamics of Multi-Phase Systems*, Blaisdell, 1967.
- [7] J. McGlaun, S. Thompson, Cth: A three-dimensional shock wave physics code, *International Journal of Impact Engineering* 10 (1990) 351–360.
- [8] D. J. Benson, A multi-material Eulerian formulation for the efficient solution of impact and penetration problems, *Comput. Mech.* 15 (1995) 558–557.
- [9] D. J. Benson, Eulerian finite element methods for the micromechanics of heterogeneous materials: Dynamic prioritization of material interfaces, *Comput. Methods Appl. Mech. Engrg.* 151 (1998) 343–360.
- [10] B. Kashiwa, A multifield model and method for fluid-structure interaction dynamics, Tech. Rep. LA-UR-01-1136, Los Alamos National Laboratory, Los Alamos (2001).
- [11] P. Saffman, On the boundary condition at the surface of a porous medium, *Studies in Appl. Math* 50 (1971) 93–101.
- [12] P. Thompson, *Compressible-fluid Dynamics*, McGraw-Hill, New York, 1972.
- [13] B. A. Kashiwa, M. L. Lewis, T. Wilson, Fluid-structure interaction modeling, Tech. Rep. LA-13111-PR, Los Alamos National Laboratory, Los Alamos (1996).
- [14] F. H. Harlow, A. A. Amsden, Numerical calculation of almost incompressible flow, *J. Comp. Phys.* 3 (1968) 80–93.
- [15] B. A. Kashiwa, R. M. Rauenzahn, A cell-centered ICE method for multiphase flow simulations, Tech. Rep. LA-UR-93-3922, Los Alamos National Laboratory, Los Alamos (1994).
- [16] D. Sulsky, Z. Chen, H. L. Schreyer, A particle method for history-dependent materials, *Comp. Methods Appl. Mech. Engrg.* 118 (1994) 179–196.

- [17] D. Sulsky, S. Zhou, H. Schreyer, Application of a particle-in-cell method to solid mechanics, *Computer Physics Communications* 87 (1995) 236–252.
- [18] J. U. Brackbill, H. M. Ruppel, Flip: A low-dissipation, particle-in-cell method for fluid flows in two dimensions, *J. Comp. Phys.* 65 (1986) 314–343.
- [19] S. Bardenhagen, J. Guilkey, K. Roessig, J. Brackbill, W. Witzel, J. Foster, An improved contact algorithm for the material point method and application to stress propagation in granular material, *Computer Modeling in Engineering and Sciences* 2 (2001) 509–522.
- [20] S. Bardenhagen, E. Kober, The generalized interpolation material point method, *Computer Modeling in Engineering and Sciences* (to appear).
- [21] F. H. Harlow, A. A. Amsden, Flow of interpenetrating material phases, *J. Comp. Phys.* 18 (1975) 440–464.
- [22] W. B. VanderHeyden, B. Kashiwa, Compatible fluxes for van leer advection, *J. Comp. Phys.* 146 (1998) 1–28.
- [23] R. Cook, W. Young, *Advanced Mechanics of Materials*, Macmillan, New York, 1985.
- [24] M. A. Saad, *Compressible Fluid Flow*, Prentice-Hall, New Jersey, 1985.
- [25] J. Guilkey, J. Weiss, Implicit time integration for the material point method: Quantitative and algorithmic comparisons with the finite element method, *International Journal for Numerical Methods in Engineering* 57 (2003) 1323–1338.